CrossMark

SCUBA-2 Ultra Deep Imaging EAO Survey (STUDIES). II. Structural Properties and Near-infrared Morphologies of Faint Submillimeter Galaxies

Yu-Yen Chang[1] , Nicholas Ferraro[1,2], Wei-Hao Wang[1] , Chen-Fatt Lim[1,3], Yoshiki Toba[1,4] , Fangxia An[5,6,7] ,
Chian-Chou Chen[8,30] , Ian Smail[5] , Hyunjin Shim[9], Yiping Ao[6,10] , Andy Bunker[11,12], Christopher J. Conselice[13] ,
William Cowley[14], Elisabete da Cunha[15] , Lulu Fan[16] , Tomotsugu Goto[17], Kexin Guo[18,19] , Luis C. Ho[18,20] ,
Ho Seong Hwang[21] , Chien-Hsiu Lee[22], Minju Lee[10,23,24] , Michał J. Michałowski[25] , I. Oteo[8,26] , Douglas Scott[27] ,
Stephen Serjeant[28] , Xinwen Shu[29], James Simpson[1,31] , and Sheona Urquhart[28]
[1] Academia Sinica Institute of Astronomy and Astrophysics, No. 1 Section 4 Roosevelt Road, 11F of Astro-Math Building, Taipei 10617, Taiwan
yuyenchang.astro@gmail.com
[2] Department of Astronomy, University of Virginia, 530 McCormick Road, Charlottesville, VA 22904, USA
[3] Graduate Institute of Astrophysics, National Taiwan University, No. 1 Section 4 Roosevelt Road, Taipei 10617, Taiwan
[4] Department of Astronomy, Kyoto University, Kitashirakawa-Oiwake-cho, Sakyo-ku, Kyoto 606-8502, Japan
[5] Centre for Extragalactic Astronomy, Department of Physics, Durham University, Durham DH1 3LE, UK
[6] Purple Mountain Observatory, Chinese Academy of Sciences, Nanjing 210008, People's Republic of China
[7] University of Chinese Academy of Sciences, Beijing 100049, People's Republic of China
[8] European Southern Observatory, Karl Schwarzschild Strasse 2, Garching, Germany
[9] Department of Earth Science Education, Kyungpook National University, 80 Daehak-ro, Buk-gu, Daegu 41566, Republic of Korea
[10] National Astronomical Observatory of Japan (NAOJ), Mitaka, Tokyo 181-8588, Japan
[11] Department of Physics, University of Oxford, Denys Wilkinson Building, Keble Road, Oxford, OX1 3RH, UK
[12] Affiliate Member, Kavli Institute for the Physics and Mathematics of the Universe, 5-1-5 Kashiwanoha, Kashiwa, 277-8583, Japan
[13] School of Physics and Astronomy, The University of Nottingham, University Park, Nottingham NG7 2RD, UK
[14] Kapteyn Astronomical Institute, University of Groningen, P.O. Box 800, NL-9700 AV Groningen, The Netherlands
[15] The Australian National University, Mount Stromlo Observatory, Cotter Road, Weston Creek, ACT 2611, Australia
[16] Shandong Provincial Key Lab of Optical Astronomy and Solar-Terrestrial Environment, Institute of Space Science, Shandong University,
Weihai, 264209, People's Republic of China
[17] Institute of Astronomy, National Tsing Hua University, Hsinchu 30013, Taiwan
[18] Kavli Institute for Astronomy and Astrophysics, Peking University, Beijing 100871, People's Republic of China
[19] International Centre for Radio Astronomy Research, University of Western Australia M468, 35 Stirling Highway, Crawley, WA 6009, Australia
[20] Department of Astronomy, School of Physics, Peking University, Beijing, People's Republic of China
[21] Quantum Universe Center, Korea Institute for Advanced Study, 85 Hoegiro, Dongdaemun-gu, Seoul 02455, Republic of Korea
[22] Subaru Telescope, NAOJ, Hilo, HI 96720, USA
[23] Department of Astronomy, The University of Tokyo, 7-3-1 Hongo, Bunkyo-ku, Tokyo 133-0033, Japan
[24] Department of Physics, Nagoya University, Furo-cho, Chikusa-ku, Nagoya 464-8602, Japan
[25] Astronomical Observatory Institute, Faculty of Physics, Adam Mickiewicz University, 60-286 Poznań, Poland
[26] Institute for Astronomy, University of Edinburgh, Royal Observatory, Blackford Hill, Edinburgh EH9 3HJ, UK
[27] Department of Physics and Astronomy, University of British Columbia, 6225 Agricultural Road, Vancouver, V6T 1Z1, Canada
[28] School of Physical Sciences, The Open University, Milton Keynes, MK7 6AA, UK
[29] Department of Physics, Anhui Normal University, Wuhu, Anhui, 241000, People's Republic of China

Abstract

We present structural parameters and morphological properties of faint 450 μm selected submillimeter galaxies (SMGs) from the JCMT Large Program, STUDIES, in the COSMOS-CANDELS region. Their properties are compared to an 850 μm selected and a matched star-forming samples. We investigate stellar structures of 169 faint 450 μm sources ($S_{450} = 2.8–29.6$ mJy; S/N > 4) at $z < 3$ using HST near-infrared observations. Based on our spectral energy distribution fitting, half of such faint SMGs ($L_{\rm IR} = 10^{11.65\pm0.98} L_\odot$) lie above the star formation rate (SFR)/stellar mass plane. The size–mass relation shows that these SMGs are generally similar to less-luminous star-forming galaxies selected by NUV $- r$ versus $r - J$ colors. Because of the intrinsic luminosity of the sample, their rest-frame optical emission is less extended than the 850 μm sources ($S_{850} > 2$ mJy) and more extended than the star-forming galaxies in the same redshift range. For the stellar mass and SFR-matched sample at $z \simeq 1$ and $z \simeq 2$, the size differences are marginal between faint SMGs and the matched galaxies. Moreover, faint SMGs have similar Sérsic indices and projected axis ratios as star-forming galaxies with the same stellar mass and SFR. Both SMGs and the matched galaxies show high fractions ($\sim$70%) of disturbed features at $z \simeq 2$, and the fractions depend on the SFRs. These suggest that their star formation activity is related to galaxy merging and the stellar structures of SMGs are similar to those of star-forming galaxies. We show that the depths of submillimeter surveys

are approaching the lower luminosity end of star-forming galaxies, allowing us to detect galaxies on the main sequence.

1. Introduction

The population known as "submillimeter galaxies" (SMGs) was first discovered using the Submillimeter Common User Bolometer Array (SCUBA; Holland et al. 1999) on the James Clerk Maxwell Telescope (JCMT) in the late 1990s in deep 850 μm images (Smail et al. 1997; Barger et al. 1998; Hughes et al. 1998). SMGs are understood to be a population of dusty starburst galaxies undergoing rapid stellar mass growth, and thus they play an important role in our understanding of galaxy evolution and formation (see reviews by Blain et al. 2002 and Casey et al. 2014).

SMGs represent sources of the most luminous galaxies ($L_{IR} \gtrsim 10^{12} L_{\odot}$; e.g., Magnelli et al. 2012; Swinbank et al. 2014) at high redshifts ($z \gtrsim 2$; e.g., Chapman et al. 2005; Simpson et al. 2014). Their high luminosities are akin to local ultra-luminous infrared galaxies (ULIRGs; see the review by Sanders & Mirabel 1996), which are almost invariably mergers. All studies of local ULIRGS morphologies converge on a very high merger fraction (Clements et al. 1996; Surace et al. 2000; Farrah et al. 2001; Veilleux et al. 2002), according to their morphology in the optical and near-infrared (NIR). However, theoretical models provide different formation routes for SMGs. They can be major mergers with significant starbursts, similar to local ULIRGs (e.g., Narayanan et al. 2010); a heterogeneous population of merger-driven starbursts and secularly evolving disk galaxies (e.g., Hayward et al. 2011); or simply represent the most massive star-forming galaxy population at high redshift (e.g., Kereš et al. 2005; Davé et al. 2010; Narayanan et al. 2015). Moreover, Lacey et al. (2016) suggested that SMGs are predominately disc-instability triggered starbursts. Additionally, using large-scale simulations, Cowley et al. (2015) found that SMGs detected in single-dish surveys can be chance superpositions of starbursting galaxies of very different redshifts along the same line of sight (see also Hayward et al. 2013; Muñoz Arancibia et al. 2015). Therefore, it is important to investigate structures and morphologies of SMGs in large submillimeter surveys to verify these different possibilities.

At high redshift, morphologies of IR-luminous galaxies (e.g., Melbourne et al. 2009; Ricciardelli et al. 2010; Bussmann et al. 2011; Zamojski et al. 2011; Alaghband-Zadeh et al. 2012; Ivison et al. 2012; Kartaltepe et al. 2012; Aguirre et al. 2013; Olivares et al. 2016; Farrah et al. 2017) and massive galaxies (e.g., Buitrago et al. 2008) have been investigated. Thanks to the high-resolution imaging available with the *Hubble Space Telescope* (*HST*), the stellar structure of SMGs has been investigated. Pope et al. (2005) used *HST*/Advanced Camera for Surveys (ACS) images to find larger sizes and a higher degree of asymmetry for 40 850 μm selected SMG. Swinbank et al. (2010) analyzed the *HST* *F*160*W*-band images of 25 radio-identified SMGs ($S_{850} = 3-15$ mJy) at $0.7 < z < 3.4$ from the Chapman et al. (2005) survey, and found that the half-light radii of the SMGs and their asymmetries are not statistically distinct from a comparison sample of star-forming

galaxies at similar redshifts. However, the intermediate Sérsic indices ($n \simeq 2$) suggest that the stellar structure of SMGs is best described by a spheroid/elliptical galaxy light distribution. Conselice et al. (2011) used *F*160*W*-band images to study massive galaxies ($M_* > 10^{11} M_{\odot}$) at $1.7 < z < 2.9$, including galaxies detected in the submillimeter, finding that there is a gradual increase in size toward lower redshifts. Targett et al. (2013) used the Cosmic Assembly Near-infrared Deep Extragalactic Legacy Survey (CANDELS; Grogin et al. 2011; Koekemoer et al. 2011) *F*160*W*-band imaging to study 24 1.1 mm and 870 μm sources ($S_{870\,\mu m} = 1.7-9.1$ mJy) at $1 < z < 3$. They found that almost all the (sub-) millimeter galaxies are well described by either a single exponential disk ($n \simeq 1$) or a multiple-component system in which the dominant constituent is disk-like. The extended structures are consistent with the sizes of other massive star-forming disks at $z \simeq 2$. Toft et al. (2014) showed that $3 < z < 6$ SMGs are consistent with being the progenitors of $z = 2$ quiescent galaxies, based on their size distributions and other properties.

More recently, observations with the Atacama Large Millimeter/submillimeter Array (ALMA) help refine the counterpart identification of single-dish samples. Chen et al. (2015) analyzed *HST* *F*160*W*-band imaging of 48 ALMA detected SMGs at $1 < z < 3$. They found that 82% of them appear to have disturbed morphologies, meaning that they are visually classified as either irregulars or interacting systems. They also found significant differences in the sizes and the Sérsic indices between $2 < z < 3$ SMGs and $z \simeq 2$ quiescent galaxies, and postulated that the majority of the $2 < z < 3$ SMGs with $S_{870} \gtrsim 2$ mJy are early/mid-stage major mergers (also see Wiklind et al. 2014; Cowie et al. 2018).

Despite all the above studies, there does not seem to be a converging picture of whether SMGs are triggered by disc instability or mergers. This might be caused by the differences in sample selections, redshift ranges, or methods of analysis. Furthermore, the previous studies focused on single-dish 850 μm or 1.1 mm selected SMGs, with typical fluxes of $S_{850} \gtrsim 2$ mJy, roughly corresponding to $L_{IR} \gtrsim 10^{12.3} L_{\odot}$ (dust temperature $T_d \simeq 30$ K). It is thus still difficult to study the variations as a function of star formation rates (SFRs) from ULIRGs, luminous infrared galaxies (LIRGs), to normal star-forming galaxies that have $L_{IR} < 10^{12} L_{\odot}$.

The JCMT SCUBA-2 instrument (Holland et al. 2013) enables 450 μm surveys that probe deeper (rms $\simeq 0.7$ mJy; $L_{IR} \simeq 5 \times 10^{11} L_{\odot}$) than the 850 μm samples because of the roughly two times higher angular resolution (FWHM $\simeq 7''$) and therefore lower confusion limit. Observations with SCUBA-2 at 450 μm can thus provide direct detections of fainter sources, and less ambiguous multi-wavelength counterpart identification. Chen et al. (2013a, 2013b) and Hsu et al. (2016) carried out SCUBA-2 450 μm surveys in various blank fields and lensing cluster fields to detect 450 μm SMGs sources at $S_{450} = 1-10$ mJy. The SCUBA-2 Cosmology Legacy Survey (S2CLS; Geach et al. 2013, 2017) and Casey et al. (2013) conducted deep 450 μm imaging in the center of the

Cosmic Evolution Survey (Scoville et al. 2007; COSMOS) field and various other fields. Roseboom et al. (2013) cross-identified 58 $450\,\mu m$ selected sources from the S2CLS sample ($\sigma_{450} = 1.5$ mJy, Geach et al. 2013) with *Spitzer* and *HST*/WFC3 data. They showed a correlation between emissivity index β and both stellar mass and effective radius. However, the depth was not sufficient to investigate faint SMGs, in the regime of more normal star-forming galaxies. Zavala et al. (2018) presented 64 sources ($\sigma_{450} \simeq 1.9$ mJy; $L_{IR} \simeq 1.5 \times 10^{12} L_{\odot}$ at $z < 4$) of the S2CLS sample in the Extended Groth Strip field. They found that the dominant component for most of the galaxies at all redshifts is a disk-like structure (a median Sérsic index $n \simeq 1.4$ and half-light radius $r_e \simeq 4.8$ kpc) by using the *HST F*160*W*-band imaging. They also showed a transition from irregular disks to disks with a spheroidal component at $z \simeq 1.4$ and suggested that SMGs are progenitors of massive elliptical galaxies.

To further expand the $450\,\mu m$ sample and to push to fainter depth ($\sigma_{450} \simeq 0.7$ mJy) and lower luminosity ($L_{IR} \simeq 5 \times 10^{11} L_{\odot}$), our team recently started a new program, the SCUBA-2 Ultra Deep Imaging EAO (East Asian Observatory) Survey (STUDIES; Wang et al. 2017). STUDIES targets the center of the COSMOS field, where there are CANDELS NIR data ideal for a morphological study. We combine all the SCUBA-2 data in the COSMOS-CANDELS region to reach a detection limit of $S_{450} \simeq 3$ mJy ($\sigma_{450} \simeq 0.7$ mJy). Moreover, the $450\,\mu m$ selection does not just enable finding fainter samples. Both the $450\,\mu m$ and the parallel deep $850\,\mu m$ observations ($\sigma_{850} \simeq 0.12$ mJy) help constrain the shape of the spectral energy distribution (SED). Our faint SMG sample therefore probes luminosities of approximately $L_{IR} > 2$–$5 \times 10^{11} L_{\odot}$ at $z = 1$–2, corresponding to SFRs of >40–$80\,M_{\odot}\,yr^{-1}$, assuming the standard Kennicutt (1998) relation, overlapping with that of optically selected normal star-forming galaxies. Therefore, we will be able to compare cool dusty galaxies to unobscured starbursts with similar redshifts, SFRs, and stellar masses. The *HST* NIR imaging across the STUDIES region enables us to investigate the stellar structures and morphological properties of these faint $450\,\mu m$ sources.

In this paper, we present morphological results based on structural analysis and visual classification for faint SMGs ($450\,\mu m$ sources) detected by STUDIES, as well as for a control sample matched to the STUDIES SMGs. The structure of this paper is as follows. We describe the data, catalog matching, and SED fitting in Section 2. We analyze the physical and structural properties in Section 3. We discuss the implications in Section 4 and summarize in Section 5. We use AB magnitudes throughout, adopt the cosmological parameters $(\Omega_M, \Omega_\Lambda, h) = (0.30, 0.70, 0.70)$, and assume the stellar initial mass function of Chabrier (2003).

2. Data

2.1. JCMT SCUBA-2 Data

In this paper, we use our extremely deep 450 and $850\,\mu m$ data obtained through the STUDIES program, as well as data from the JCMT archive. A full description of STUDIES is given by Wang et al. (2017), but we give a brief description here. STUDIES is a multi-year JCMT Large Program, aiming to reach the confusion limit and an rms noise below 0.6 mJy at $450\,\mu m$ in the COSMOS-CANDELS region. In this paper, we include the first 2 years of data from STUDIES (170 hr). We

also include the extremely deep archival data from the JCMT Legacy Program, S2CLS (Geach et al. 2013, 150 hr, program code: MJLSC01), and the shallower but wider archival data of Casey et al. (2013, 20 hr, program code: M11BH11A, M12AH11A, and M12BH21A). The Casey et al. (2013) data do not substantially increase the depth in the area covered by STUDIES and S2CLS, but provide a wider area for us to expand the sample size at the bright end. The data reduction and source extraction are identical to those described in Wang et al. (2017). The final combined $450\,\mu m$ map as shown in Figure 1 achieves an rms sensitivity of 0.7 mJy in its center. The areas that have rms sensitivities better than 1 mJy and 5 mJy are $\sim$10 arcmin^2 and $\sim$30 arcmin^2, respectively. For the $850\,\mu m$ map, the areas that have rms sensitivities better than 0.12 mJy and 0.15 mJy are $\sim$10 arcmin^2 and $\sim$30 arcmin^2, respectively.

2.2. Sample Selection and Catalog Matching

In our combined map, there are 248 $450\,\mu m$ sources detected above 4σ[32] ($\sigma_{450} < 5$ mJy) with a wide range of flux densities (2.8 mJy $< S_{450} < 29.6$ mJy with a median value of 6.4 mJy). In the same area, there are 128 $850\,\mu m$ sources ($\sigma_{850} < 1$ mJy) above 2 mJy. The different cuts at $450\,\sigma m$ and $850\,\sigma m$ are due to their different confusion limits. Cowie et al. (2017) determined that the confusion limit at $850\,\mu m$ is $\simeq 1.65$ mJy from their deep $850\,\mu m$ map (see also Geach et al. 2017). Although our $850\,\mu m$ map is slightly deeper than that in Cowie et al. (2017), here we conservatively select sources above 2 mJy to be free from the confusion effect. Above this 2 mJy limit, all our $850\,\mu m$ sources have S/N > 6 and 2.0 mJy $< S_{850} < 16.7$ mJy.

We used photometry from the optical to far-infrared (FIR) in the COSMOS2015 catalog (Laigle et al. 2016). First, we matched the $450\,\mu m$ sources with sources in the VLA 3 GHz catalog (Delvecchio et al. 2017; Smolčić et al. 2017) using a 4″ search radii. (Expected false match rate, the expected number of objects that are mismatched over the total number of the sample, based on the number density of the population and the search area, is $\simeq 0.02$.) Among the 248 $450\,\mu m$ detected sources, 132 sources are matched to a VLA 3GHZ counterpart (see Figure 2). Then we used the VLA positions to find counterparts in the COSMOS2015 catalog. For the remaining $450\,\mu m$ sources, we matched them with mid-infrared (MIR) $24\,\mu m$ sources (Le Floc'h et al. 2009) using 4″ search radii (expected false match rate $\simeq 0.09$), and 80 sources are found (Figure 2). We then used 3″ search radii to cross-match the $24\,\mu m$ sources with *Spitzer* IRAC sources. After that, we used the IRAC positions to find the counterparts in the COS-MOS2015 catalog. As a result, there are 198 $450\,\mu m$ sources (expected false match rate $\simeq 0.04$) with COSMOS2015 counterparts.

For the $850\,\mu m$ sources, we first matched them with the $450\,\mu m$ sources with 8″ search radii (expected false match rate $\simeq 0.09$). We also matched $450\,\mu m$ undetected $850\,\mu m$ sources with the VLA catalog using 7″ search radii (expected false match rate $\simeq 0.07$) and used the VLA positions to find their COSMOS2015 counterparts. A total of 77 counterparts can be found with this cross-matching method.

---

[32] According to Figure 9 in Wang et al. (2017), the expected spurious fraction is around 1%–10% for the sample at 20–4 mJy. The confusion limit is around 1–2 mJy (e.g., Chen et al. 2013a; Geach et al. 2013; Wang et al. 2017).
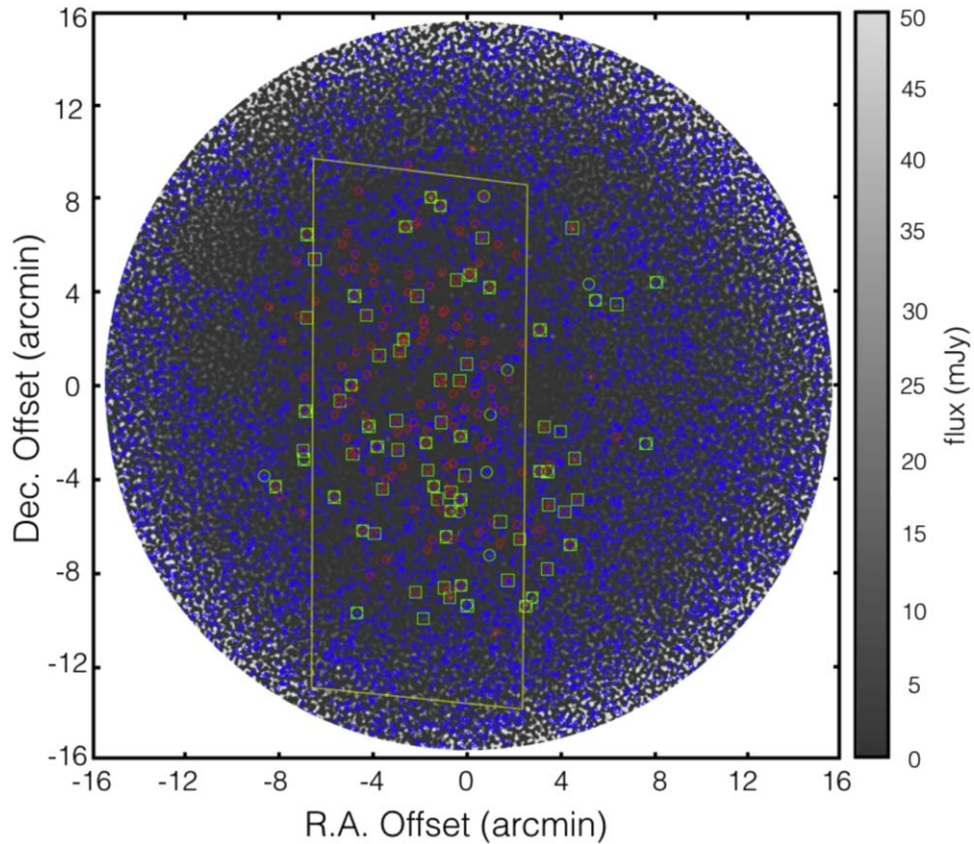
Figure 1. STUDIES 450 μm flux map that provides coverage over $\simeq$700 arcmin^2 centered at R.A. = 10:00:22.26, decl. = +02:24:05.06. We show our sample selection of 450 μm sources (red circles with 10$''$ in radii, S/N > 4, S_{450} > 2 mJy) and 850 μm sources (green circles with 15$''$ in radii, S/N > 6, S_{850} > 2 mJy) from the machine-learning method, 850 μm sources (green box, S/N > 6, S_{850} > 2 mJy) from the cross-matched method, along with the comparison sample (blue circles with 5$''$ in radii, M_* > 10^{10} $M_\odot$, NUV − r vs. r − J selection). We consider star-forming galaxies inside the STUDIES coverage as the comparison sample. The yellow region shows the CANDELS footprint.
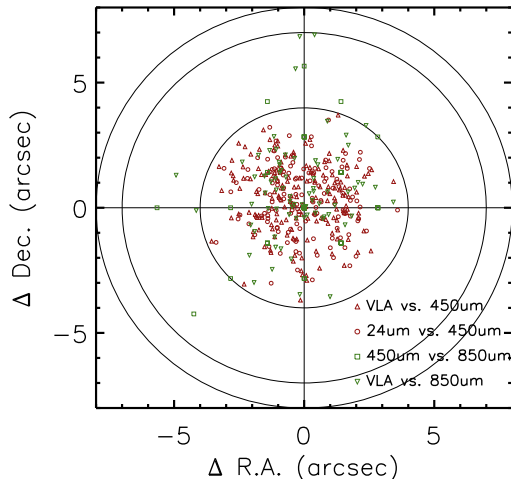

Figure 2. Offsets of the coordinates between the SMG sources and their counterparts: VLA vs. 450 μm, 24 μm vs. 450 μm, 450 μm vs. 850 μm, and VLA vs. 850 μm. The circles are search radii of 4$''$, 7$''$, and 8$''$.

We also employ the machine-learning technique to identify optical counterparts of 850 μm single-dish sources (F. An et al. 2018, in preparation). The machine-learning method identifies the likely multi-wavelength counterparts to single-dish-detected submillimeter sources by utilizing a training set of precisely located SMGs from ALMA follow-up of the SCUBA-2 Cosmology Legacy Survey's UKIDSS-UDS field

(AS2UDS). The precision of the machine-learning classification is 82%, as shown in An et al. (2018). In our work, the precision reaches 88% (An et al. 2018, private communication) because we adopt a smaller search radius (5$''$) to match the machine-learning classified counterparts to 850 μm sources.

There are 44 near-infrared detected galaxies classified as the counterparts of 850 μm sources by the machine-learning method. Among them, 39 850 μm single-dish sources have a counterpart identified by the machine-learning and the cross-matched method mentioned above. Among the 39 sources, 36 of them (>92%) lead to the same optical counterparts. The main results in this work are not changed whether we use solely the cross-matched sample, solely the machine-learning sample, or both samples. As a result, we adopt the 44 machine-learning classifications as 850 μm counterparts, and then include an additional 39 cross-matched 850 μm sources that do not have any counterparts in the machine-learning method (Figure 1). Overall, there are 83 850 μm sources (expected false match rate $\simeq$0.07) with COSMOS2015 counterparts.

Among the 248 450 μm sources and 128 850 μm sources, 50 (20%) and 44 (34%), respectively, do not have any radio, MIR, or machine-learning counterparts. A plausible explanation for the unidentified sources is that the radio and MIR observations are not deep enough at high redshift. The SMG population may start to drop outside the 3 GHz and 24 μm detection limits above $z \sim 3$, as shown in Figure 3. The unidentified sources are likely to be at $z > 3$, but we cannot

Table 1
List of 188 SMGs Sources (169 450 and 80 850 μm Optical-matched Sources)

ID	z	R.A. (deg)	Decl. (deg)	S_{450} (mJy)	S/N$_{450}$	S_{850} (mJy)	S/N$_{850}$	M_* ($M_\odot$)	SFR ($M_\odot$ yr^{-1})	R_e (kpc)	q	n
611035	1.03	150.07354	2.22639	22.19	4.48	⋯	⋯	10.83 ± 0.10	1.47 ± 0.12	7.56 ± 0.07	0.65 ± 0.00	1.04 ± 0.02
616608	2.15	150.12496	2.23698	8.29	3.52	2.23	6.18	10.33 ± 0.06	2.03 ± 0.10	6.84 ± 0.17	0.22 ± 0.01	0.20 ± 0.02
619287	2.03	150.17187	2.24070	⋯	⋯	2.84	6.46	11.13 ± 0.03	1.53 ± 0.14	3.22 ± 0.36	0.82 ± 0.02	1.64 ± 0.15
623330	1.85	150.09406	2.24590	8.60	3.81	2.87	8.86	10.17 ± 0.00	2.26 ± 0.00	5.81 ± 0.08	0.29 ± 0.01	0.51 ± 0.02
623536	2.31	150.05248	2.24560	22.74	6.19	6.38	12.21	11.37 ± 0.09	2.51 ± 0.08	⋯	⋯	⋯

Note. Here we show their IDs (COSMOS2015), photometric redshifts (COSMOS2015), coordinates (COSMOS2015), 450 μm fluxes, 450 μm signal-to-noise ratios, 850 μm flux, 850 μm signal-to-noise ratios, stellar masses, SFRs, effective radii, projected axis ratios, and Sérsic indices.

(This table is available in its entirety in machine-readable form.)
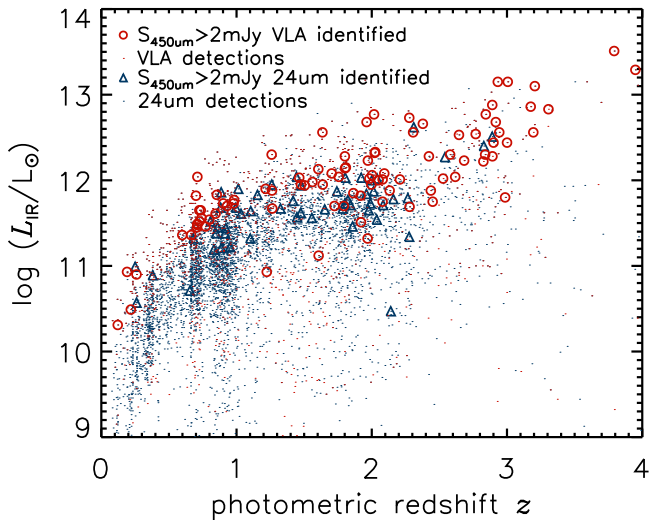

Figure 3. Photometric redshift to infrared luminosity plot for 450 μm sources identified by VLA and 24 μm position (red circles and blue triangles), as well as VLA and 24 μm detections (red and blue points, which are not 450 μm detections). The infrared luminosity is derived by MAGPHYS (see Section 2.4 for more details).

confirm this until we have deeper radio and/or MIR observations or direct ALMA imaging.

In our sample, we remove infrared and X-ray selected (L_X(2–10 keV) > 10^{42} erg s^{-1}) AGNs that are identified by previous work (Civano et al. 2016; Marchesi et al. 2016; Chang et al. 2017a, 2017b). Among the sources with COSMOS2015 counterparts identified with the above procedure, there are 169 450 μm detected sources and 80 850 μm detected sources with reliable COSMOS2015 photometric redshifts (a precision of $\sigma_{\Delta z/(1+z_s)} = 0.034$ and a catastrophic failure fraction of $\eta = 10\%$ for $z \sim 2$ sources according to Laigle et al. 2016). We finally reach a sample of 188 sources that are detected at either 450 or 850 μm, or both, and have photometric redshifts. These are listed in Table 1. We note that 64 of the sources in our sample are detected at both 450 and 850 μm. There are 31 out of 188 SMGs with high confidence level spectroscopic redshifts (Lilly et al. 2007) in the COSMOS spectroscopic master catalog (M. Salvato et al. 2018, in preparation). These spectroscopic redshifts, the photometric redshifts of our SMGs, are highly reliable (a precision of $\sigma_{\Delta z/(1+z_s)} = 0.024$ and a catastrophic failure fraction of $\eta = 3\%$). Therefore, we adopt the COSMOS2015 photometric redshifts in this paper.

We identified star-forming galaxies across the STUDIES image using the COSMOS catalog and a NUV $-$ r versus

$r - J$ selection (see Ilbert et al. 2013 for more details). To perform a fair comparison, we only considered the 69,820 star-forming galaxies that are located in the same area (700 arcmin^2) as our JCMT sample (Figure 1) and are not classified as STUDIES SMGs. In this way, for all the star-forming galaxies undetected by SCUBA-2, we can set upper limits for their 450 and 850 μm flux densities for the SED fitting in Section 2.4.

To define our comparison sample of star-forming galaxies, we removed sources identified as SMGs. However, at the high SFR end, some of these STUDIES-undetected star-forming galaxies might be still somewhat bright at 450 μm. They were not detected simply because of the incompleteness of our source extraction and the shallower depth in the outer part of our 450 μm image. To test if our normal star-forming galaxies are significantly contaminated by dusty SMGs that lie just below our 450 μm detection threshold, we conducted stacking analyses. For star-forming galaxies with SFR >100 $M_\odot$ yr^{-1} at $z = 1$–3, we obtained a stacked flux of 0.96 ± 0.23 mJy, or approximately three times lower than the faintest 450 μm sources in our SMG sample. We therefore conclude that there is not significant SMG contamination in our comparison sample. As a side note, what is interesting here is the obscured SFR in these galaxies. The above stacked 450 μm flux corresponds to an infrared luminosity of $L_{IR} = 1.6 \times 10^{11} L_\odot$ and thus an obscured SFR of 26 $M_\odot$ yr^{-1}. This is much smaller than their mean total SFR of 166 $M_\odot$ yr^{-1} estimated by MAGPHYS, and implies that the majority of their star formation is unobscured and is seen in the rest-frame UV.

2.3. CANDELS Imaging

CANDELS (Grogin et al. 2011; Koekemoer et al. 2011) is an *HST* Multi-Cycle Treasury Program using the Wide Field Camera 3 (WFC3) in the NIR *F125W* and *F160W* bands to target five legacy fields (COSMOS, GOODS-N, GOODS-S, UDS, and EGS). In the COSMOS field (Nayyeri et al. 2017), covers 9′ × 24′ to a limit of $H \simeq 27$ mag (*F160W*, 5σ). The CANDELS imaging has been reduced and drizzled to a 0″06 pixel scale and high-resolution (FWHM ≃ 0″2) mosaics. In the CANDELS region (yellow polygon in Figure 1), 139 out of our 169 450 μm sources with redshifts and 58 out of our 80 850 μm sources with redshifts can be matched to CANDELS sources, among the 38,671 CANDELS sources in the COSMOS field (van der Wel et al. 2012; Nayyeri et al. 2017) detected with SExtractor (Bertin & Arnouts 1996). For the comparison sample, 19,197 star-forming galaxies are matched to the CANDELS catalog. We are considering optical light of dusty sources. At $z > 3$, *F160W* imaging traces

rest-frame emission at $<0.4\,\mu$m from galaxies. Therefore we focus on $z < 3$ sources in this paper. This leaves 128 $450\,\mu$m sources, 46 $850\,\mu$m sources, and 17,108 compared star-forming galaxies for our stellar structural analysis.

2.4. SED Fitting

We model the observed photometry of our SMGs and the $NUV - r$ versus $r - J$ star-forming sample with the Multi-wavelength Analysis of Galaxy Physical Properties (MAG-PHYS) code (da Cunha et al. 2008). MAGPHYS computes the emission from the stellar populations in galaxies from UV to NIR consistently with the emission from dust at MIR and FIR wavelengths using an energy balance technique. We use the version of the MAGPHYS code that has been modified for sources at high redshifts (see da Cunha et al. 2015). In the fitting, we included photometry from COSMOS2015 (optical: u, B, V, i^+, z^{++}; MIR: Y, J, H, K_s, 3.6, 4.5, 5.8, 8.0, 24 μm; FIR: 70, 100, 160, 250, 350, 500 μm; with the choice of aperture ($3''$) and corrections identical to those used in Chang et al. 2017a) as well as 450 and $850\,\mu$m flux densities from the SCUBA-2 images.

For sources that are undetected by SCUBA-2, we adopt 4σ upper limits, and the higher value between 2 mJy (confusion limit) and 6σ as the upper limit at $850\,\mu$m. Figure 4 shows two examples of the SMG photometry and SED fitting. We derive the stellar mass ($M_\star$), SFR, specific SFR (sSFR = SFR$/M_\star$), and infrared luminosity (dust luminosity at 3–2000 μm defined by MAGPHYS) from the SED fitting. The typical infrared luminosity of our faint SMGs ($450\,\mu$m selected sources) is $10^{11.7}\,L_\odot$ (mean $L_{\rm IR} = 10^{11.65\pm0.98}\,L_\odot$; median $L_{\rm IR} = 10^{11.77}\,L_\odot$), which places these sources between the LIRG ($L_{\rm IR} > 10^{11}\,L_\odot$) and ULIRG ($L_{\rm IR} > 10^{12}\,L_\odot$) limits, as shown in Figure 3.

The SED fitting significantly underestimates the infrared luminosities of some of the sources (see Figure 3), so we visually inspected their SEDs. We found that this is a result at both low significant photometry and catastrophic failure by MAGPHYS, which fits the optical and IR photometry simultaneously. The latter is probably because the dominant optical and IR emissions of these galaxies do not come from the same physical regions (see Simpson et al. 2017; Calistro Rivera et al. 2018 for a recent example) and therefore the energy balance for the UV and FIR in MAGPHYS breaks down. For significantly underestimated ($>4\sigma$ at 450 or $850\,\mu$m) sources ($\simeq$10%), we fitted the optical and infrared parts of the SEDs separately. Their SFRs are replaced by the sum of the infrared SFR and uncorrected UV SFR according to Kennicutt (1998) and Kennicutt & Evans (2012). In rare cases (4%) where both the MAGPHYS fitting and our infrared fitting fail to reproduce the observed photometries (at 450 and $850\,\mu$m) within 4σ, the problem seems to lie in the photometries themselves. We thus remove those sources from our sample.

In this paper, we randomly select five star-forming galaxies with stellar mass and SFR (or sSFR) within 0.1 dex of every $450\,\mu$m SMG, in the same redshift bin as their comparison sample. However, we note that for $z \simeq 2$, 26% $\pm$ 2% of the matched star-forming galaxies are included two to four times because of the limited sample size at the high stellar mass end. Therefore, we include these uncertainties by bootstrapping in our analyses.

3. Analysis

3.1. Star-forming Sequence

In order to investigate the star formation process in dusty galaxies compared to the general galaxy population, we compare our sample with the star-forming sequence (stellar mass versus SFR, also called "main sequence;" e.g., Brinchmann et al. 2004; Daddi et al. 2007; Elbaz et al. 2007; Noeske et al. 2007; Chang et al. 2015; Ilbert et al. 2015; Schreiber et al. 2015). Based on our SED fitting results, we define our own star-forming sequence at different redshifts in Figure 5 (black solid lines). Here we only include galaxies with reasonable SED fitting results by visually inspecting them and deciding an empirical choice of reduced chi-square value ($\chi^2 < 50$) in the MAGPHYS output files. There are 159 (out of 188) such SMGs, and the stellar masses and SFRs are listed in Table 1.

With the same sample selection for star-forming galaxies, the median difference between COSMOS2015 and our SED fitting results are small (-0.01 dex for stellar masses and 0.07 for SFRs). We also show the main sequence relations from Whitaker et al. (2014) and Speagle et al. (2014). However, our SFR estimations are generally lower than those in the literature by $\sim$0.7 dex. The main reason might be selection of the star-forming sample, since our median values are close to the COSMOS2015 catalogs with the same sample selection. Moreover, our SFRs would be higher if we consider 24 μm or *Herschel* selected sample. To avoid bias from different selection criteria, we use the $NUV - r$ versus $r - J$ selection, but show the literature in Figure 5 for comparison. The SFR differences between the various works are more significant at the high stellar mass end, so it is important to compare SMGs with star-forming galaxies using SFRs derived with the same method.

In Figure 5 and Table 2, we show that the SMGs are above or on our star-forming sequence (i.e., an SFR that is higher than or similar to most of the population at that stellar mass) for both 450 and $850\,\mu$m sources at all redshifts. If we define the star-forming sequence spanning ±0.3 dex around our median values, about half (48% $\pm$ 5%) of the faint SMGs ($450\,\mu$m sources) lie above the main sequence, and half (43% $\pm$ 4%) of them are on the main sequence.

3.2. GALFIT Measurements

We investigate the stellar structure of the STUDIES SMGs that lie in the CANDELS/COSMOS region. We adopt the structural parameters of $HST/F160W$-selected sources in the CANDELS field for available NIR filters ($F160W$ and $F125W$) in van der Wel et al. (2012). The best-fitting single-component Sérsic models are produced by GALFIT (Peng et al. 2010). According to van der Wel et al. (2012), a precision and accuracy of 20% or better can be reached for measurements of the effective radius ($R_{\rm e}$) and projected axis ratio (q) for $H < 24.5$ (75% of our sample) and Sérsic index (n; the degree of curvature of the Sérsic profile) for $H < 23.5$ (60% of our sample) at typical CANDELS depth. In our structural and morphological analyses, we only consider STUDIES sources detected at $H < 24.5$ (for $R_{\rm e}$ and q) or $H < 23.5$ (for n), ensuring that the desired properties are both highly precise and accurate.

In order to show the rest-frame optical size dependence on magnitude and infrared luminosity, we chose two typical redshift ranges in Figure 6. Both the $z \simeq 2.2$ sample at $F160W$
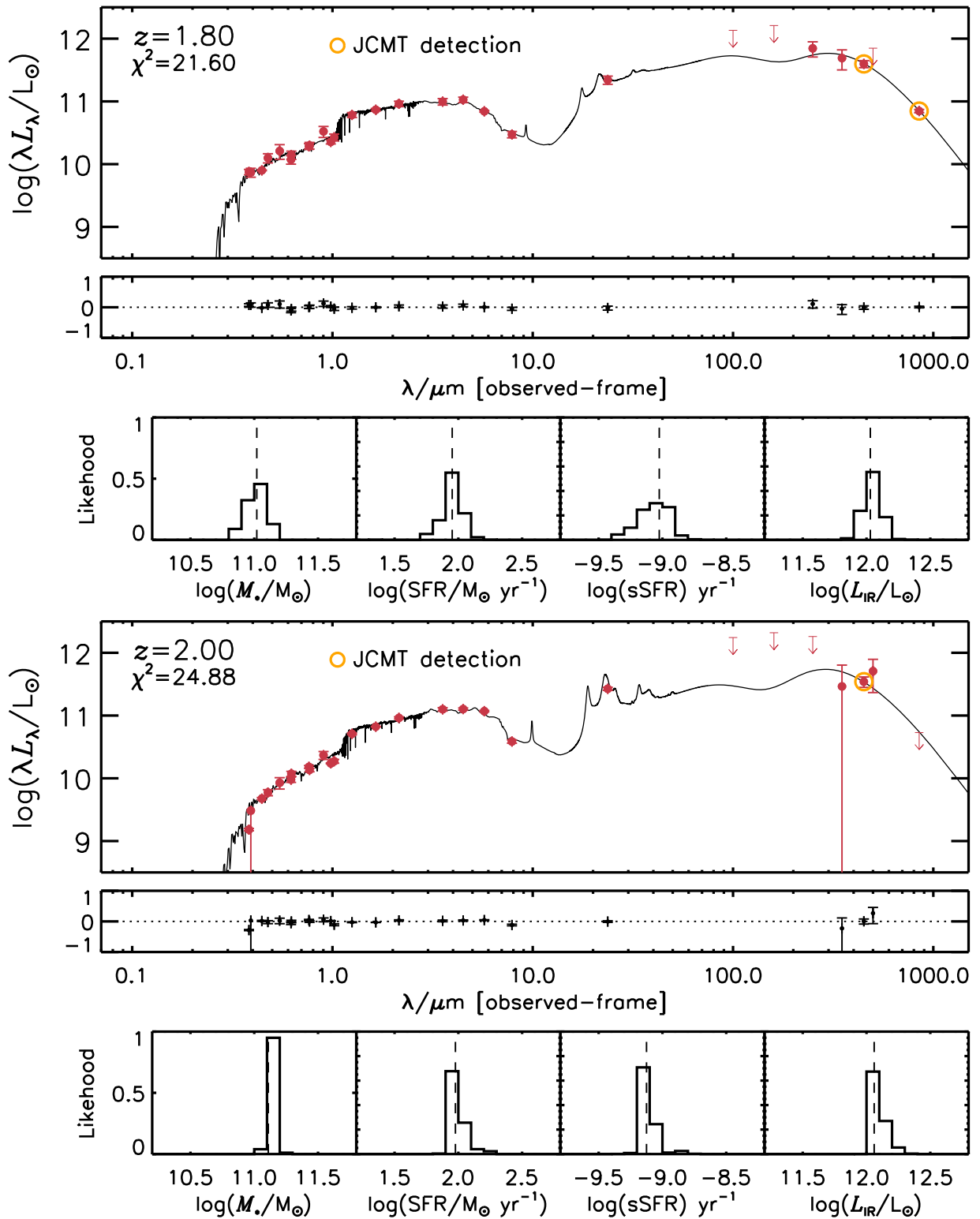
Figure 4. Two typical SED fitting examples for 450 μm detected sources. The red points are the photometry, and the red arrows are the upper limit of the photometry. The black lines show the best-fitting template. The orange circles label the JCMT detections. The upper example has both 450 and 850 μm detection, and the lower example has only 450 μm detection. The residuals and histograms of the physical parameters (stellar mass, SFR, sSFR, and infrared luminosity) are shown in the lower panels. In the histograms, the dashed lines are the median values.

and the $z \simeq 1.5$ sample at $F125W$ correspond to a rest-frame wavelength of 5000 Å. For the 450 μm sources, the $z \simeq 2.2$ sample tends to have smaller sizes than the $z \simeq 1.5$ sample. This trend of smaller sizes and lower redshift is consistent with

the known size evolution of the overall galaxy population from $z \simeq 3$ to our local universe (e.g., Barro et al. 2013, 2014; van der Wel et al. 2014). The median sizes of 450 μm sources are slightly larger than normal star-forming galaxies at the same
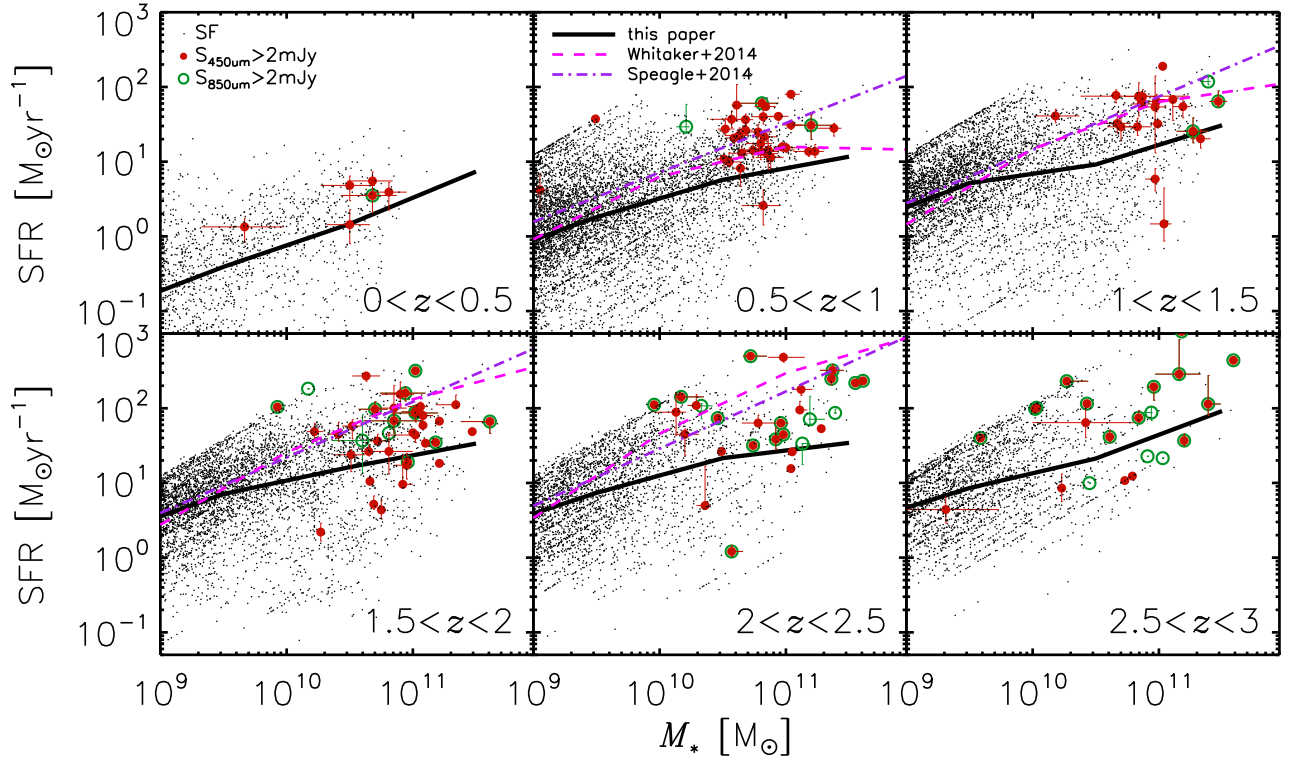
Figure 5. Stellar mass vs. SFR relation at $z < 3$ for 450 μm detected sources (red), 850 μm sources (green), and a sample of star-forming galaxies (black). The values are derived from our SED fitting. Most of the SMGs lie on or above the star-forming sequence. The black solid lines are median SFRs of star-forming galaxies in bins of 0.5 dex of stellar mass. We also show the sequences derived by Whitaker et al. (2014; magenta dash lines) and Speagle et al. (2014; purple dashed-dotted lines).

Table 2
The Median Values of Stellar Masses and SFRs of $M_* > 10^{10} M_\odot$ Galaxies in Figure 5

Samples	$0 < z < 0.5$	$0.5 < z < 1$	$1 < z < 1.5$	$1.5 < z < 2$	$2 < z < 2.5$	$2.5 < z < 3$
			$\log(M_*/M_\odot)$			
Star-forming Galaxies	10.32 ± 0.01	10.39 ± 0.02	10.42 ± 0.02	10.38 ± 0.02	10.35 ± 0.02	10.27 ± 0.01
850 μm sources	10.68 ± 0.00	10.81 ± 0.30	11.39 ± 0.10	10.95 ± 0.00	10.97 ± 0.01	10.93 ± 0.01
450 μm sources	10.68 ± 0.09	10.82 ± 0.01	10.97 ± 0.02	10.94 ± 0.01	10.94 ± 0.04	10.76 ± 0.00
			$\log(SFR/M_\odot\, yr^{-1})$			
Star-forming Galaxies	0.17 ± 0.02	0.78 ± 0.02	1.01 ± 0.03	1.24 ± 0.03	1.36 ± 0.03	1.33 ± 0.04
850 μm sources	0.55 ± 0.00	1.49 ± 0.16	1.81 ± 0.20	1.88 ± 0.06	1.90 ± 0.01	2.00 ± 0.01
450 μm sources	0.59 ± 0.02	1.32 ± 0.01	1.73 ± 0.01	1.69 ± 0.03	1.83 ± 0.01	2.00 ± 0.00

Note. The uncertainties are estimated by bootstrapping.

magnitude and infrared luminosity. In general, Figure 6 shows that the general population of 450 μm sources follow the most luminous end of normal star-forming galaxies. Therefore, we derive the effective radius (R_e) at a rest-frame wavelength of 5000 Å according to Equation (1)[33] in van der Wel et al. (2014), which considers the wavelength dependence of R_e as a function of redshift and galaxy stellar mass. In Figure 7, we compare our stellar mass to size relation with that inferred by van der Wel et al. (2014; see their Figure 5). Most of the SMGs are similar in size (for their stellar mass) to star-forming galaxies at all redshifts.

We then consider high accuracy objects ($H < 24.5$ for the effective radius) over the range $1.5 < z < 2.5$. The median effective radius is 4.26 ± 0.05 kpc, and the mean is 4.68 ± 0.09 kpc for 450 μm sources, while the median is 4.38 ± 0.07 kpc, and the mean is 5.28 ± 0.10 kpc for 850 μm sources, compared with a median of 3.13 ± 0.12 kpc and a mean of 3.86 ± 0.12 kpc for a stellar mass and SFR matched sample to the 450 μm galaxies. The uncertainties here and below are estimated from a bootstrapping analysis. A Kolmogorov-Smirnov (K-S) test shows that the matched star-forming sample is marginally different from both the 450 and the 850 μm samples ($P_{K-S} \simeq 0.05$). The 850 μm sample seems to be more extended than the 450 μm sample, probably because they are more luminous and massive sources. The sample sizes are not large enough to show significant differences with the K-S test ($P_{K-S} \simeq 0.95$).
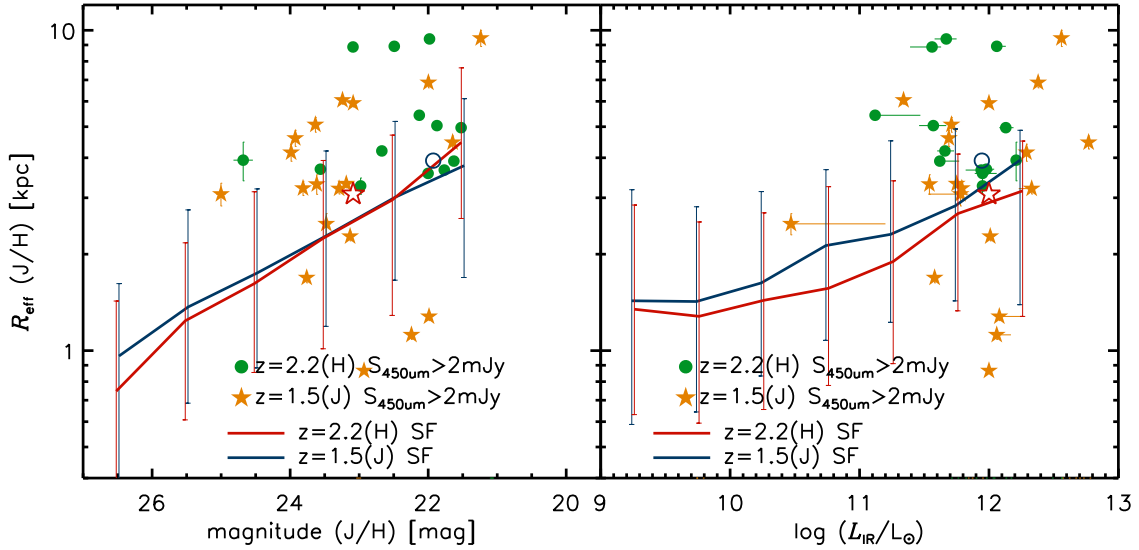
---

[33] $R_e = R_{e,F} \left(\frac{1+z}{1+z_p} \right)^{\frac{\Delta \log R_e}{\Delta \log \lambda}}$, where F denotes either F125W ($z < 1.5$) or F160W ($z > 1.5$), and z_p is the pivot redshift for these respective filters (1.5 for F125W and 2.2 for F160W). In addition, $\frac{\Delta \log R_e}{\Delta \log \lambda} = -0.35 + 0.12z - 0.25 \log \left(\frac{M_*}{10^{10} M_\odot} \right)$, where M_* is the stellar mass.

Figure 6. Size to magnitude and infrared luminosity plot. Here we show the effective radius and magnitude at $F160W$ for $z \simeq 2.2$ sample (orange star: 450 μm sources) and at $F125W$ for $z \simeq 1.5$ sample (green circle: 450 μm sources). The near-infrared observations correspond to a rest-frame wavelength of 5000 Å. The 16th, 50th, and 84th percentiles of size for the star-forming galaxies are shown at different magnitude and infrared luminosity bins. The median values of 450 μm detected sources are labeled as red stars ($z \simeq 2.2$) and blue circles ($z \simeq 1.5$).
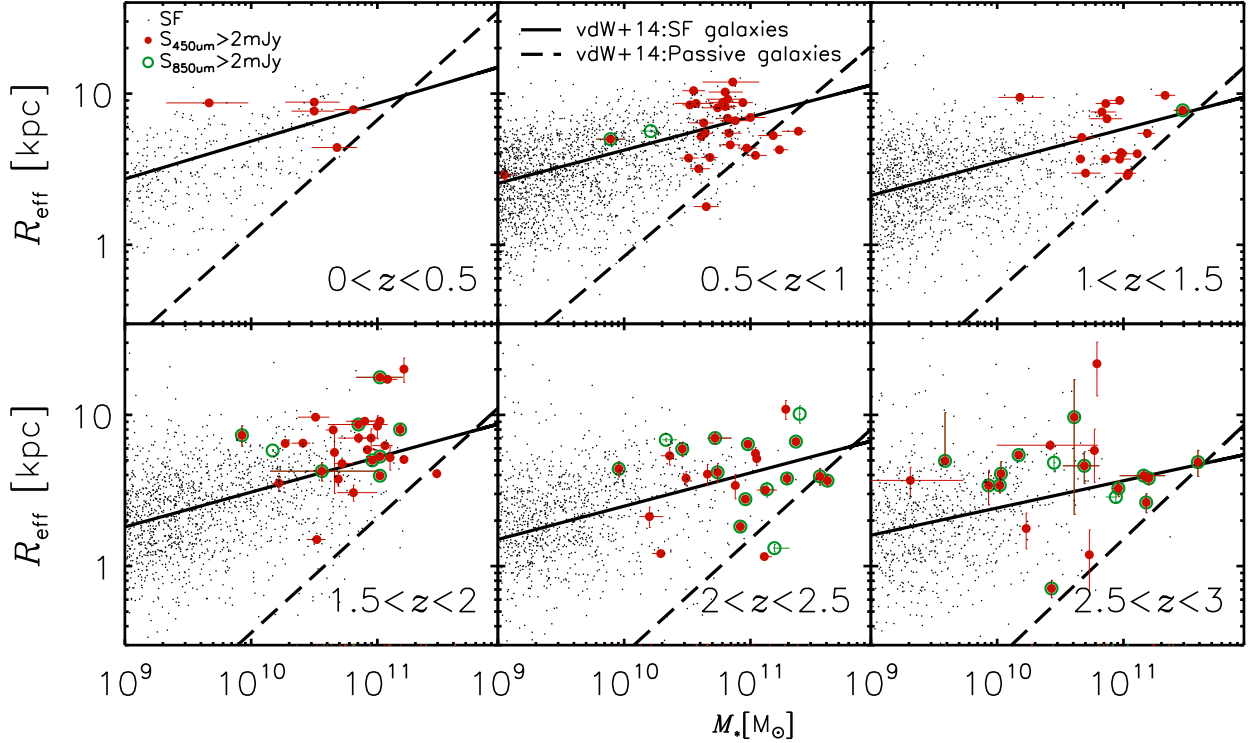
Figure 7. Stellar mass vs. size relation at $z < 3$ for 450 μm detected sources, 850 μm detected sources, and a comparison sample of star-forming galaxies. The black lines are fitted to normal star-forming and passive galaxies in van der Wel et al. (2014). Most of the SMGs are similar to star-forming galaxies, rather than passive galaxies.

In the lower redshift range $0.5 < z < 1.5$, the median effective radius is 4.90 ± 0.26 kpc and the mean is 5.55 ± 0.10 kpc for the 450 μm sources, while the median is 4.85 ± 0.61 kpc and the mean is 4.07 ± 0.07 kpc for the 850 μm sources, compared with a median of 4.28 ± 0.09 kpc and a mean of 4.75 ± 0.09 kpc for the 450 μm matched sample. The sizes of both the 450 μm and the matched sample at $z \simeq 1$ are larger than those at $z \simeq 2$, which is

consistent with the usual size evolution of galaxies (e.g., Toft et al. 2007; Zirm et al. 2007; van Dokkum et al. 2008; Newman et al. 2012; van der Wel et al. 2014). However, the sample size of the 850 μm sources is too small to constrain the $z \simeq 1$ population. On the other hand, the effective radius of the 450 μm sample seems to be larger than the matched sample, although the difference is not significant, ($P_{K-S} \simeq 0.49$).
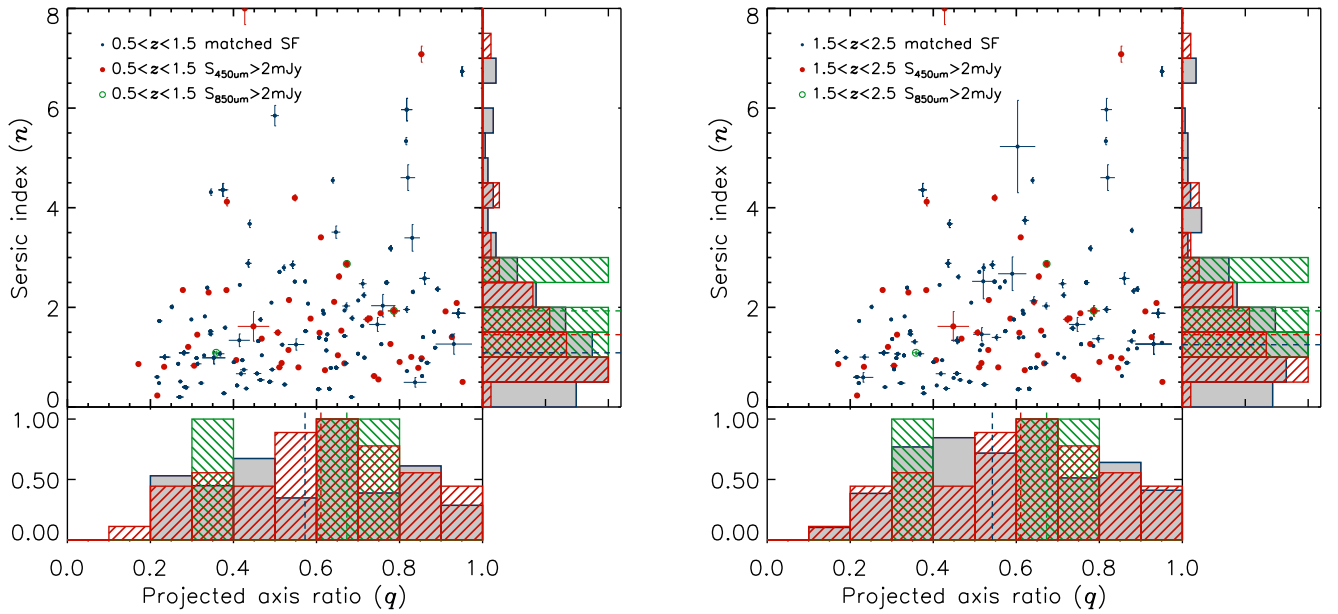
Figure 8. Sérsic index and axis ratio measured in the *F160W* band (*H* < 23.5) for the 450 μm selected sources, 850 μm selected sources, and a comparison sample of stellar mass and SFR-matched star-forming galaxies at $0.5 < z < 2.5$ and $1.5 < z < 2.5$. In the histograms, the dash lines show the median values. There is no significant differences ($P_{K-S} > 0.05$) between the SMGs and the matched sample.
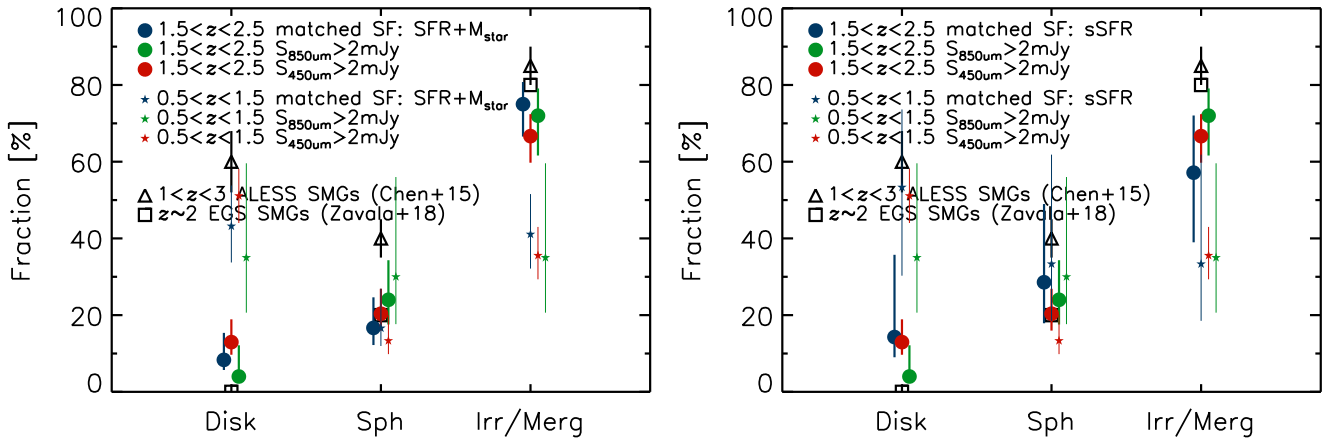

Figure 9. Visual classification of the 450 μm detected sources and 850 μm sources. The comparison star-forming galaxies are matched to stellar mass and SFR (left panel), as well as sSFR (right panel). Most of the SMGs contain merger features, similarly or slightly more frequently than the comparison sample. The error bars represent the 68.3% binomial confidence limits, as described in Cameron (2011). For comparison, we show the visual classifications of SMGs provided by Chen et al. (2015) and Zavala et al. (2018). The higher fractions of disks and spheroids in the literature are because of their non-mutually exclusive classifications.

In Figure 8, we show the Sérsic index versus the projected axis ratio measured in the *F160W* band for sources brighter than $H = 23.5$ (the Sérsic index measurement limit). For the comparison sample, we matched the stellar masses and SFRs of star-forming galaxies with the available 450 μm sources ($H < 23.5$) in the same diagram. At $z \simeq 2$, the median Sérsic index is 1.08 ± 0.07 and the mean is 1.79 ± 0.06 for the 450 μm sources, while the median is 0.86 ± 0.06 and the mean is 1.67 ± 0.06 for the 850 μm sources, compared with a median of 1.30 ± 0.05 and a mean of 1.96 ± 0.06 for the comparison sample. At $z \simeq 1$, the median Sérsic index is 1.45 ± 0.03 and the mean is 1.80 ± 0.04 for the 450 μm sources, while the median is 1.93 ± 0.88 and the mean is 1.96 ± 0.03 for the 850 μm sources, compared with a median of 1.22 ± 0.03 and a mean of 1.60 ± 0.04 for the comparison sample. However, according to the K-S test, there are little differences ($P_{K-S} > 0.05$) between the SMGs (both the 450 and

850 μm selected sources) and the matched star-forming galaxies for their Sérsic index and projected axis ratio.

3.3. Visual Classification

We create a stellar-mass-matched sample of star-forming galaxies to the STUDIES sources ($H < 24.5$) to investigate their morphology visually. We use the *HST* WFC3 *F160W*-band, WFC3 *F125W*-band, and ACS *F814W*-band images to study as presented in the Appendix. Due to the limited sample size at $z \simeq 3$, we focus on $z \simeq 1$ and $z \simeq 2$ sources in this subsection.

First, we compared visual classification of the SMGs with that of stellar mass and SFR-matched star-forming galaxies. We classify them as disks, spheroids, and irregular/mergers. The fractions of these classes are presented in the left panel of Figure 9. These classes are mutually exclusive, so the classification represents the dominant morphology. All the
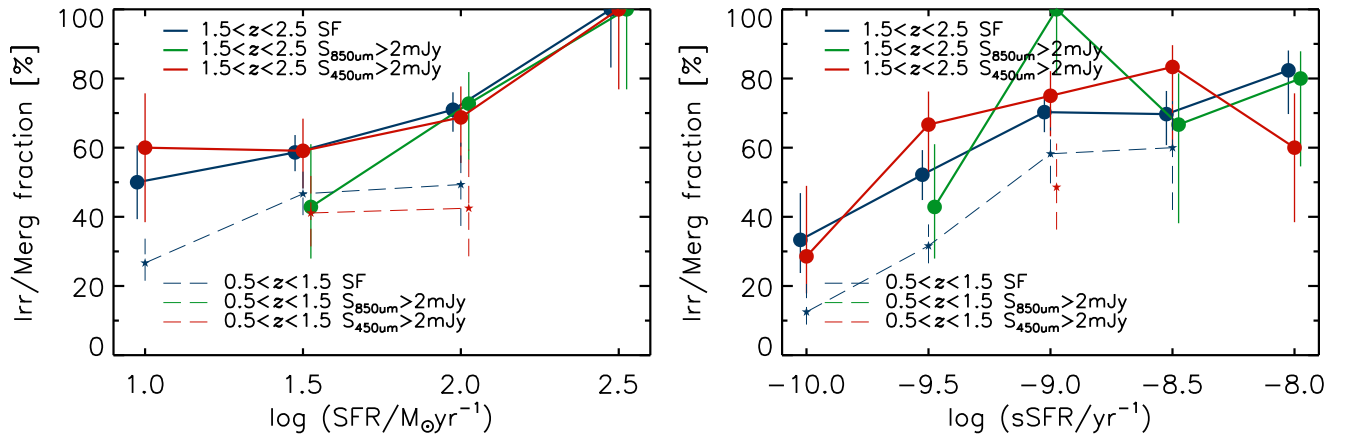
Figure 10. Disturbed feature fraction vs. SFR and sSFR for 450 μm sources, 850 μm sources, and a comparison sample of $M_* > 10^{10} M_\odot$ star-forming galaxies at $1.5 < z < 2.5$. This shows that disturbed features depend on the SFRs for all types of galaxy. The error bars here represent the 68.3% binomial confidence limits, as described in Cameron (2011). We also show the classifications of previous SMGs by Chen et al. (2015) and Zavala et al. (2018).

sources are examined by five classifiers (Y.Y.C., F.F., W.H.W., C.F.L., and Y.T.). The error bar in each classification class represents the 68.3% (1-σ) confidence limits, derived with the method described in Cameron (2011), which estimates the confidence intervals for a population with a Bayesian approach. In the left panel of Figure 9, most of the SMGs have merger or disturbed features (irregular galaxies). However, the stellar mass and SFR-matched star-forming sample also show a comparably high disturbed feature fraction. The classifiers used a strict definition for the class of irregular/mergers, which includes weak perturbed features. We also checked that the disturbed feature fractions of the SMGs and the comparison sample are still comparable and high if we conducted a less strict classification. Such high fractions could be explained by early- to mid-stage major mergers. There is a hint of an elevated disturbed feature fraction in the 850 μm sample compared to the 450 μm sample and the normal star-forming galaxies. However, the difference between the 850 μm sample and the star-forming galaxies is 2σ, and thus statistically insignificant. In Figure 9, we also show previous $F160W$-band visual classification results. Chen et al. (2015) classified ALESS SMGs to five non-mutually exclusive classes: disk, spheroid, irregular, unresolved, and unclassified by four classifiers. Zavala et al. (2018) used a visual-like classification from Huertas-Company et al. (2015), which is based on neutral networks trained to reproduce the visual morphologies by Kartaltepe et al. (2015). Though the definition of classes are not the same, the high disturbed feature fractions are consistent with our results.

In order to investigate whether the disturbed feature fraction depends on SFR, we consider a comparison sample of $M_* > 10^{10} M_\odot$ star-forming galaxies that lie at the same redshift as the SMGs. In the left panel of Figure 10, we show that the fraction of disturbed sources correlates with SFR for the 450, 850 μm, and comparison sample. At $z \simeq 2$, the fraction goes up mildly with SFR, although there are no clear distinctions among the disturbed feature fractions of the three samples at any given SFR. Using the star-forming sample, we find the disturbed feature fraction as a function of SFR to be $f_{\rm irr/merg}(\%) = (32 \pm 8) + (11 \pm 15) \times \log[{\rm SFR}/(M_\odot {\rm yr}^{-1})]$, where $f_{\rm irr/merg}$ is the irregular/merger fraction. Moreover, the correlations are very strong (Pearson correlation coefficient

>0.96) for all the samples. The disturbed fraction does not seem to depend on how dusty the starbursts are; the dependence only seems to be on SFR. At $z \simeq 1$, disturbed feature fractions are lower than those at $z \simeq 2$, as shown in Figure 9. A possible reason is that our selection at 450 and 850 μm identifies more massive and luminous sources at $z \simeq 2$ (Figure 3). Though the disturbed feature fractions of $z \simeq 1$ sources are slightly lower at fixed SFR, it is still difficult to conclude any redshift dependence due to the limited sample sizes. Nevertheless, both $z \simeq 1$ and $z \simeq 2$ samples show correlations between disturbed feature fractions and their star formation in Figure 10.

In parallel, we checked an sSFR (=SFR/M_*) matched sample that is randomly selected using five star-forming galaxies within 0.1 dex in sSFR of every 450 μm SMG at the same redshift bin. In the right panel of Figure 9, we find that the disturbed feature fractions of SMGs are higher than that of the sSFR-matched sample. In the right panel of Figure 10, the correlation of the 450 μm sources is still strong (Pearson correlation coefficient >0.80), but not as strong as that of the sSFR-matched galaxies (Pearson correlation coefficient >0.98).

4. Discussion

4.1. How Do SMGs Compare with Normal Galaxies in the Star-forming Sequence?

According to our stellar mass and SFR estimation, most of the SMGs are on or slightly above the star-forming sequence, as shown in Figure 5. Despite a decade of observational study, the location of the most luminous, 850 μm selected SMGs relative to the star-forming main sequence remains hotly debated. Indeed, various studies into the properties of luminous SMGs have concluded that these systems either represent starburst galaxies, which lie significantly above the main sequence (e.g., da Cunha et al. 2015; Danielson et al. 2017), or conversely, that they simply represent the massive "tip" of the known main sequence (Koprowski et al. 2016; Michałowski et al. 2017). The reason for these discrepant results can typically be traced to systematic uncertainties on the measurement of stellar mass, which is strongly affected by different assumptions on the star formation history (Hainline et al. 2011; Michałowski et al. 2012, 2014). STUDIES allows us to extend

such studies to a sample of faint 450 μm sources. In Table 1, the stellar masses and SFRs of the STUDIES 450 μm sources are lower than those of 850 μm sources at $z < 2.5$. The main reason is that the SED peak of typical $z \sim 2$ SMGs is around 200–400 μm and 450 μm observations can detect less-luminous SMGs compared to 850 μm observations. However, 450 μm detected galaxies still have higher stellar mass and SFRs than normal star-forming galaxies.

Can our result that SMGs lie slightly above the star-forming sequence be a consequence of overestimated SFRs? *Herschel* observations may overestimate FIR fluxes (and hence SFRs) of dusty galaxies due to source clustering (Hwang et al. 2010; Wang et al. 2017) within coarse resolution (15″–35″ FWHM) of SPIRE imaging at 250–500 μm. Attempt to correct for this flux bias requires either a complete set of prior positions for deblending (e.g., Swinbank et al. 2014) or assumptions for the properties of the underlying population (e.g., Béthermin et al. 2012; Harris et al. 2016).

To test this, we conducted SED fitting by using only SPIRE (optical+*Spitzer*+PACS+SPIRE) and only SCUBA-2 (optical+*Spitzer*+PACS+SCUBA-2) data in the FIR bands. The resulting mean SFR offset is 4% with a scatter of 9% for SPIRE-detected sources (S/N > 3 at 250, 350, or 500 μm). The difference is relatively small because MAGPHYS estimates SFRs by considering photometry from UV to FIR wavelengths. The overestimation can be larger if SFRs are derived monochromatically from SPIRE and SCUBA-2 fluxes. In order to avoid such a bias in the SED fitting of our comparison sample, we also considered the upper limits at 450 μm for them. On the other hand, because *Herschel* fluxes are included in their SED fitting and the SCUBA-2 450 μm photometry is not deep enough for most of them, it is still possible that their SFRs are overestimated in Figure 5. However, this scenario would further strengthen our finding that the SMGs from our deep 450 μm survey can be on or slightly above the star-forming galaxies on the SFR–M_* plane.

We find that 450 μm selected SMGs ($S_{450} = 2.8$–29.6 mJy; S/N > 4 at $z < 3$) are on or slightly above the star-forming sequence. This result seems robust against potential biases in the estimations of the SFR of our SMG and comparison samples. It is commonly assumed that galaxies above the sequence are undergoing merger-induced starbursts. However, Cowley et al. (2017) show that dynamically triggered star formation (e.g., merger/disc-instability) does not necessarily segregate galaxies on the SFR–M_* plane, which may also help explain the half-on half-off results on the star-forming sequence. Hence even for the SMGs on the star-forming sequence, there may be additional dynamical processes occurring, such as merging. Therefore, in the next subsection, we will turn our focus to the stellar structure of SMGs and look for evidence of merging and interaction.

We examined the source density and SFR density per comoving volume for $z = 1$–3. Above 200 $M_\odot$ yr^{-1}, the SMG sample dominates over the normal galaxy sample in terms of both source density and SFR density, but the sample sizes are small for both samples. When we go down to >100 $M_\odot$ yr^{-1}, the normal galaxy sample becomes roughly twice as large as the SMG sample, but their integrated SFR densities are comparable. Below 100 $M_\odot$ yr^{-1}, the normal galaxy sample strongly dominates in both the source density and SFR density.

It is now clear that once we probe down to SFR of $\sim$100 $M_\odot$ yr^{-1}, we see both obscured galaxies (appearing as SMGs) and unobscured galaxies (appearing in the optical sample). Above this limit, SMGs are dominant, and below this, normal galaxies are dominant. Therefore, from the points of view of morphology (the topic of this paper), SED (obscured versus unobscured star formation as tested with stacking analyses), and comoving SFR density, we see that as we go deeper in the submillimeter, we start to enter the regime where normal galaxies play more important roles or dusty galaxies become less important. This is also in concordance with our 450 μm counts (Wang et al. 2017), which suggest that we can fully account for the 450 μm background once we can detect faint sources of roughly 0.5–0.8 mJy. As we further deepen and widen our 450 μm map, we will publish better constrained faint-end counts at 450 μm. We also defer a complete SED analyses of 450 μm sources versus normal galaxies to a future paper. All these should help better understand how ultraluminous dusty galaxies are connected to normal star-forming galaxies and their relative contribution to the cosmic star formation history.

4.2. Structures of Dusty Galaxies

The stellar mass to size relation in Figure 7 shows that the sizes of SMGs are similar to those of star-forming galaxies, rather than passive galaxies. In general, 850 μm sources are more extended (larger and flatter) than the 450 μm sources, and 450 μm sources are more extended than normal star-forming galaxies. The larger spatial extent of the 850 μm sources can be understood through their higher luminosities and stellar masses. Extended stellar structures were also found in previous SMG studies (e.g., Smail et al. 2000; Swinbank et al. 2010; Targett et al. 2013; Chen et al. 2015).

The slight difference in size might be explained if the NUV − r versus r − J selections of the star-forming sample are contaminated by passive galaxies. However, such contamination can be removed using the SFR estimated from our SED fitting. After matching the stellar mass and SFR, we still find a small difference in size between our SMGs and the comparison sample at $z \sim 2$, as discussed in Section 3.2. A plausible explanation for the mild size difference is dust extinction. Recent high-resolution ALMA imaging shows that dust continuum emission from SMGs and massive star-forming galaxies is quite compact, compared to their NIR stellar continuum emission (e.g., Ikarashi et al. 2015; Simpson et al. 2015; Hodge et al. 2016; Iono et al. 2016; Tadaki et al. 2017; Calistro Rivera et al. 2018). Even if SMGs and normal star-forming galaxies are comparable in the sizes of their stellar components, the highly extincted cores caused by the compact dust components could bias the measured effective radii outward. More sophisticated analyses are clearly required to further investigate this possibility, including spatially resolved SED fitting for dust extinction and stellar mass, and high-resolution ALMA imaging for low SFR galaxies, as well as multi-wavelength image simulations. Such studies may explain the lack of obvious difference in Sérsic index and projected axis ratio between SMGs and the matched sample (as shown in Figure 8).

Figure 9 shows that most SMGs (around 70%) contain irregular/merger features. We find that the irregular/merger fraction is positively correlated with the SFR (Figure 10). Moreover, the comparison sample, which is plausibly less obscured, behaves identically to the submillimeter selected sample. Given the high SFRs of 850 μm sources (as shown in

Section 3.1), it is thus natural to see them having the highest disturbed feature fraction in Figure 9. This is consistent with previous morphological studies of submillimeter samples (e.g., Chapman et al. 2003; Conselice et al. 2003; Swinbank et al. 2010; Wiklind et al. 2014; Chen et al. 2015; Cowie et al. 2018).

The dependence on sSFR is consistent with that of Hung et al. (2013), who showed that the fraction of interacting merger systems increases with the deviation from star-forming sequence. Moreover, Hwang et al. (2011) also demonstrated that galaxy-galaxy interactions and mergers have been strongly affecting SFRs by using *Herschel* data. Unlike the result for the SFR, we see slightly different behaviors of the irregular/ merger fractions with sSFR between the SMGs and the matched sample. The disturbed feature fraction of SMGs seems to be higher than an sSFR-matched sample, as shown in the right panels of Figures 9 and 10. What this implies is that for galaxies of the same sSFR, those in merging/disturbed systems tend to be more luminous at 450 or 850 μm, while the undisturbed ones tend to have lower dust obscuration. A naive explanation is that merging systems tend to have more compact star-forming regions in their cores (as revealed in many recent ALMA observations), while undisturbed systems tend to have disk-wide star formation. The small spatial extent of dusty star-forming regions in the merging/disturbed systems then lead to stronger extinction in the UV and thus stronger dust re-radiation in the FIR and submillimeter. This scenario again remains to be tested with more observations and simulations. We also caution that the differences in irregular/merger fractions are far from huge ($72^{+7}_{-10}\%$, $67^{+6}_{-7}\%$, $57^{+15}_{-18}\%$ for 850 μm sources, 450 μm sources, and sSFR-matched star-forming galaxies, respectively), and are statistically insignificant, indicating that even if merging events play a role in triggering SMGs among galaxies with the same sSFR, they are probably not the only factor (Hayward et al. 2011).

In addition to having the high SFRs and sSFRs, SMGs also have globally low dust temperature and high attenuation (according to our SED fitting; see also Magnelli et al. 2012). Therefore, we checked dependence of the frequency of merger related features on dust temperature and attenuation. We found that the Pearson correlation coefficients are not high (0.05 for dust temperature and 0.11 for attenuation), as opposed to the value for SFR versus disturbed feature fraction (>0.96). Most SMGs do have disturbed features, but the disturbed feature fraction mainly depends on the SFR. This suggests that galaxy merging takes place in bright galaxies with high SFRs and can be related to star formation activity. According to our structural and morphological analyses, dusty galaxies are very similar to star-forming galaxies in the rest-frame optical bands. Recently, several SMGs were imaged at high resolution by ALMA, and the results appear to be mixed. Some of them show clumpy and extended structures (i.e., disk-like; e.g., Iono et al. 2016), while others show starbursts in compact regions (e.g., Fujimoto et al. 2017; Oteo et al. 2017) or irregular morphologies (e.g., Miettinen et al. 2017). These results show a great variation in the structure of dusty emitting regions in SMGs, and future observations are required to quantify the prevalence of different morphologies in a thorough manner. Moreover, recent findings show that the stellar morphologies of luminous SMGs appear significantly more extended and disturbed than their ALMA dust images at $z \sim 2.5$ (Hodge et al. 2016; Chen et al. 2017; Calistro Rivera et al. 2018). Given these diverse results, it is clear that further investigations of the dust and stellar morphologies of SMGs are necessary.

To summarize, we have found that faint SMGs selected with deep 450 μm observations have stellar structures similar to those of less-luminous star-forming galaxies in the optical sample in terms of Sérsic index, projected axis ratio, and fraction of galaxies with perturbed features. The 450 μm sources are slightly more extended than normal star-forming galaxies and also lie on or slightly above the star-forming sequence, but these small differences might be a consequence of various selection effects or dust extinction. There is less similarity between the normal star-forming galaxies and the more luminous 850 μm selected SMGs, in terms of sizes of the stellar distribution. These results show that as our submillimeter surveys approach the lower luminosity end ($<10^{12} L_\odot$), we start to detect normal galaxies on the main sequence statistically.

5. Summary

In this paper, we have investigated physical and structural properties of SMGs in the NIR, especially for a faint 450 μm sample selected from our extremely deep STUDIES image. Our main findings are as follows.

1. 450 μm selected SMGs are located above or on the star-forming sequence at $z < 3$. If we define the star-forming sequence as being within ± 0.3 dex around the median values, about half ($48\% \pm 5\%$) of the faint SMGs (450 μm selected sources) lie above the main sequence, and half ($43\% \pm 4\%$) are on the main sequence.

2. SMGs are similar to star-forming galaxies in the size–mass relation at $z < 3$.

3. As a result of the intrinsic luminosity of each sample, the 850 μm sources are typically extended than 450 μm sources, and 450 μm sources are more extended than normal star-forming galaxies, in terms of the apparent sizes of their stellar components. For the stellar mass and SFR-matched sample, the size differences are only marginal between faint SMGs and the comparison galaxies. Such a minor difference may be explained by the sizes of their dusty regions.

4. SMGs have similar Sérsic index and projected axis ratios to star-forming galaxies with the same stellar mass and SFR at $z \simeq 2$.

5. Both SMGs and the matched star-forming sample show a high fraction ($\sim 80\%$) of disturbed features, and the irregular/merger fractions of both SMGs and normal star-forming galaxies show similar SFR dependence.

6. Our results suggest that galaxy merging can be related to star formation activity, and stellar structures of SMGs are similar to normal star-forming galaxies of comparable stellar mass.

7. Among SMGs and normal star-forming galaxies of similar sSFR, merging/disturbed systems tend to appear in the submillimeter sample as dusty sources, while undisturbed systems tend to show up in the optical sample. However, the tendency is not strong, indicating that galaxy merging is not the only factor in the triggering of SMGs.

8. Our results based on the STUDIES data show that as submillimeter surveys approach lower luminosities

$(<10^{12} L_\odot)$, we start to detect large samples of normal galaxies that lie on the main sequence at $z < 3$.

Appendix
NIR Imaging of SMGs

Figure 11 shows an example of NIR imaging of SMG. The complete figure set is available in the online journal.
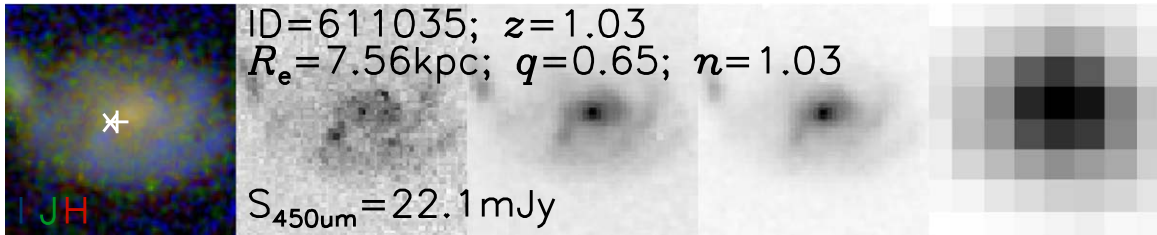

Figure 11. Cutouts of the SMGs in Table 1 if the NIR images are available. COSMOS2015 611035 is shown as an example; the complete figure set (149 images) is available in the online journal. The five panels are true color images (modified from the code by Lupton et al. 2004), *HST*/ACS *I*-band, along with the *HST*/WFC3 *F*125*W*-band, *HST*/WFC3 *F*160*W*-band, and IRAC (3.6 μm) images. The box size is 6 arcsec × 6 arcsec, and the center is the optical counterpart in COSMOS2015. The positions of VLA 3 GHz (x symbol) and 24 μm counterparts (plus symbol) for 450 μm sources are also labeled in the true color images. The COSMOS2015 ID, photometric redshift (z), effective radius (R_e), projected axis ratio (q), Sérsic index (n), 450 μm flux density, and 850 μm flux density are also given.

(The complete figure set (149 images) is available.)

ORCID iDs

Yu-Yen Chang ⓘ https://orcid.org/0000-0002-6720-8047
Wei-Hao Wang ⓘ https://orcid.org/0000-0003-2588-1265
Yoshiki Toba ⓘ https://orcid.org/0000-0002-3531-7863
Fangxia An ⓘ https://orcid.org/0000-0001-7943-0166
Chian-Chou Chen ⓘ https://orcid.org/0000-0002-3805-0789
Ian Smail ⓘ https://orcid.org/0000-0003-3037-257X
Yiping Ao ⓘ https://orcid.org/0000-0003-3139-2724
Christopher J. Conselice ⓘ https://orcid.org/0000-0003-1949-7638
Elisabete da Cunha ⓘ https://orcid.org/0000-0001-9759-4797
Lulu Fan ⓘ https://orcid.org/0000-0003-4200-4432
Kexin Guo ⓘ https://orcid.org/0000-0001-6103-2821
Luis C. Ho ⓘ https://orcid.org/0000-0001-6947-5846
Ho Seong Hwang ⓘ https://orcid.org/0000-0003-3428-7612
Minju Lee ⓘ https://orcid.org/0000-0002-2419-3068
I. Oteo ⓘ https://orcid.org/0000-0001-5875-3388
Douglas Scott ⓘ https://orcid.org/0000-0002-6878-9840
Stephen Serjeant ⓘ https://orcid.org/0000-0002-0517-7943
Xinwen Shu ⓘ https://orcid.org/0000-0002-7020-4290
James Simpson ⓘ https://orcid.org/0000-0002-8521-1995

References

Aguirre, P., Baker, A. J., Menanteau, F., Lutz, D., & Tacconi, L. J. 2013, ApJ, 768, 164
Alaghband-Zadeh, S., Chapman, S. C., Swinbank, A. M., et al. 2012, MNRAS, 424, 2232
An, F. X., Stach, S. M., Smail, I., et al. 2018, ApJ, 862, 101
Barger, A. J., Cowie, L. L., Sanders, D. B., et al. 1998, Natur, 394, 248
Barro, G., Faber, S. M., Pérez-González, P. G., et al. 2013, ApJ, 765, 104
Barro, G., Faber, S. M., Pérez-González, P. G., et al. 2014, ApJ, 791, 52
Bertin, E., & Arnouts, S. 1996, A&AS, 117, 393
Béthermin, M., Le Floc'h, E., Ilbert, O., et al. 2012, A&A, 542, A58
Blain, A. W., Smail, I., Ivison, R. J., Kneib, J.-P., & Frayer, D. T. 2002, PhR, 369, 111
Brinchmann, J., Charlot, S., White, S. D. M., et al. 2004, MNRAS, 351, 1151
Buitrago, F., Trujillo, I., Conselice, C. J., et al. 2008, ApJL, 687, L61
Bussmann, R. S., Dey, A., Lotz, J., et al. 2011, ApJ, 733, 21
Calistro Rivera, G., Hodge, J. A., Smail, I., et al. 2018, ApJ, 863, 56
Cameron, E. 2011, PASA, 28, 128
Casey, C. M., Chen, C.-C., Cowie, L. L., et al. 2013, MNRAS, 436, 1919
Casey, C. M., Narayanan, D., & Cooray, A. 2014, PhR, 541, 45
Chabrier, G. 2003, PASP, 115, 763
Chang, Y.-Y., Le Floc'h, E., Juneau, S., et al. 2017a, ApJS, 233, 19
Chang, Y.-Y., Le Floc'h, E., Juneau, S., et al. 2017b, MNRAS, 466, L103
Chang, Y.-Y., van der Wel, A., da Cunha, E., & Rix, H.-W. 2015, ApJS, 219, 8
Chapman, S. C., Blain, A. W., Smail, I., & Ivison, R. J. 2005, ApJ, 622, 772
Chapman, S. C., Windhorst, R., Odewahn, S., Yan, H., & Conselice, C. 2003, ApJ, 599, 92
Chen, C.-C., Cowie, L. L., Barger, A. J., et al. 2013a, ApJ, 762, 81
Chen, C.-C., Cowie, L. L., Barger, A. J., et al. 2013b, ApJ, 776, 131
Chen, C.-C., Hodge, J. A., Smail, I., et al. 2017, ApJ, 846, 108
Chen, C.-C., Smail, I., Swinbank, A. M., et al. 2015, ApJ, 799, 194
Civano, F., Marchesi, S., Comastri, A., et al. 2016, ApJ, 819, 62
Clements, D. L., Sutherland, W. J., McMahon, R. G., & Saunders, W. 1996, MNRAS, 279, 477
Conselice, C. J., Bluck, A. F. L., Buitrago, F., et al. 2011, MNRAS, 413, 80
Conselice, C. J., Chapman, S. C., & Windhorst, R. A. 2003, ApJL, 596, L5
Cowie, L. L., Barger, A. J., Hsu, L.-Y., et al. 2017, ApJ, 837, 139
Cowie, L. L., Gonzalez-Lopez, J., Barger, A. J., et al. 2018, arXiv:1805.09424
Cowley, W. I., Béthermin, M., Lagos, C. d. P., et al. 2017, MNRAS, 467, 1231
Cowley, W. I., Lacey, C. G., Baugh, C. M., & Cole, S. 2015, MNRAS, 446, 1784
da Cunha, E., Charlot, S., & Elbaz, D. 2008, MNRAS, 388, 1595
da Cunha, E., Walter, F., Smail, I. R., et al. 2015, ApJ, 806, 110
Daddi, E., Dickinson, M., Morrison, G., et al. 2007, ApJ, 670, 156
Danielson, A. L. R., Swinbank, A. M., Smail, I., et al. 2017, ApJ, 840, 78
Davé, R., Finlator, K., Oppenheimer, B. D., et al. 2010, MNRAS, 404, 1355
Delvecchio, I., Smolčić, V., Zamorani, G., et al. 2017, A&A, 602, A3
Elbaz, D., Daddi, E., Le Borgne, D., et al. 2007, A&A, 468, 33

Farrah, D., Petty, S., Connolly, B., et al. 2017, ApJ, 844, 106
Farrah, D., Rowan-Robinson, M., Oliver, S., et al. 2001, MNRAS, 326, 1333
Fujimoto, S., Ouchi, M., Shibuya, T., & Nagai, H. 2017, ApJ, 850, 83
Geach, J. E., Chapin, E. L., Coppin, K. E. K., et al. 2013, MNRAS, 432, 53
Geach, J. E., Dunlop, J. S., Halpern, M., et al. 2017, MNRAS, 465, 1789
Grogin, N. A., Kocevski, D. D., Faber, S. M., et al. 2011, ApJS, 197, 35
Hainline, L. J., Blain, A. W., Smail, I., et al. 2011, ApJ, 740, 96
Harris, K., Farrah, D., Schulz, B., et al. 2016, MNRAS, 457, 4179
Hayward, C. C., Behroozi, P. S., Somerville, R. S., et al. 2013, MNRAS, 434, 2572
Hayward, C. C., Kereš, D., Jonsson, P., et al. 2011, ApJ, 743, 159
Hodge, J. A., Swinbank, A. M., Simpson, J. M., et al. 2016, ApJ, 833, 103
Holland, W. S., Bintley, D., Chapin, E. L., et al. 2013, MNRAS, 430, 2513
Holland, W. S., Robson, E. I., Gear, W. K., et al. 1999, MNRAS, 303, 659
Hsu, L.-Y., Cowie, L. L., Chen, C.-C., Barger, A. J., & Wang, W.-H. 2016, ApJ, 829, 25
Huertas-Company, M., Gravet, R., Cabrera-Vives, G., et al. 2015, ApJS, 221, 8
Hughes, D. H., Serjeant, S., Dunlop, J., et al. 1998, Natur, 394, 241
Hung, C.-L., Sanders, D. B., Casey, C. M., et al. 2013, ApJ, 778, 129
Hwang, H. S., Elbaz, D., Dickinson, M., et al. 2011, A&A, 535, A60
Hwang, H. S., Elbaz, D., Magdis, G., et al. 2010, MNRAS, 409, 75
Ikarashi, S., Ivison, R. J., Caputi, K. I., et al. 2015, ApJ, 810, 133
Ilbert, O., Arnouts, S., Le Floc'h, E., et al. 2015, A&A, 579, A2
Ilbert, O., McCracken, H. J., Le Fèvre, O., et al. 2013, A&A, 556, A55
Iono, D., Yun, M. S., Aretxaga, I., et al. 2016, ApJL, 829, L10
Ivison, R. J., Smail, I., Amblard, A., et al. 2012, MNRAS, 425, 1320
Kartaltepe, J. S., Dickinson, M., Alexander, D. M., et al. 2012, ApJ, 757, 23
Kartaltepe, J. S., Mozena, M., Kocevski, D., et al. 2015, ApJS, 221, 11
Kennicutt, R. C., & Evans, N. J. 2012, ARA&A, 50, 531
Kennicutt, R. C., Jr. 1998, ApJ, 498, 541
Kereš, D., Katz, N., Weinberg, D. H., & Davé, R. 2005, MNRAS, 363, 2
Koekemoer, A. M., Faber, S. M., Ferguson, H. C., et al. 2011, ApJS, 197, 36
Koprowski, M. P., Dunlop, J. S., Michałowski, M. J., et al. 2016, MNRAS, 458, 4321
Lacey, C. G., Baugh, C. M., Frenk, C. S., et al. 2016, MNRAS, 462, 3854
Laigle, C., McCracken, H. J., Ilbert, O., et al. 2016, ApJS, 224, 24
Le Floc'h, E., Aussel, H., Ilbert, O., et al. 2009, ApJ, 703, 222
Lilly, S. J., Le Fèvre, O., Renzini, A., et al. 2007, ApJS, 172, 70
Lupton, R., Blanton, M. R., Fekete, G., et al. 2004, PASP, 116, 133
Magnelli, B., Lutz, D., Santini, P., et al. 2012, A&A, 539, A155
Marchesi, S., Civano, F., Elvis, M., et al. 2016, ApJ, 817, 34
Melbourne, J., Bussman, R. S., Brand, K., et al. 2009, AJ, 137, 4854
Michałowski, M. J., Dunlop, J. S., Cirasuolo, M., et al. 2012, A&A, 541, A85
Michałowski, M. J., Dunlop, J. S., Koprowski, M. P., et al. 2017, MNRAS, 469, 492
Michałowski, M. J., Hayward, C. C., Dunlop, J. S., et al. 2014, A&A, 571, A75
Miettinen, O., Delvecchio, I., Smolčić, V., et al. 2017, A&A, 606, A17
Muñoz Arancibia, A. M., Navarrete, F. P., Padilla, N. D., et al. 2015, MNRAS, 446, 2291
Narayanan, D., Hayward, C. C., Cox, T. J., et al. 2010, MNRAS, 401, 1613
Narayanan, D., Turk, M., Feldmann, R., et al. 2015, Natur, 525, 496
Nayyeri, H., Hemmati, S., Mobasher, B., et al. 2017, ApJS, 228, 7
Newman, A. B., Ellis, R. S., Bundy, K., & Treu, T. 2012, ApJ, 746, 162
Noeske, K. G., Weiner, B. J., Faber, S. M., et al. 2007, ApJL, 660, L43
Olivares, V., Treister, E., Privon, G. C., et al. 2016, ApJ, 827, 57
Oteo, I., Zwaan, M. A., Ivison, R. J., Smail, I., & Biggs, A. D. 2017, ApJ, 837, 182
Peng, C. Y., Ho, L. C., Impey, C. D., & Rix, H.-W. 2010, AJ, 139, 2097
Pope, A., Borys, C., Scott, D., et al. 2005, MNRAS, 358, 149
Ricciardelli, E., Trujillo, I., Buitrago, F., & Conselice, C. J. 2010, MNRAS, 406, 230
Roseboom, I. G., Dunlop, J. S., Cirasuolo, M., et al. 2013, MNRAS, 436, 430
Sanders, D. B., & Mirabel, I. F. 1996, ARA&A, 34, 749
Schreiber, C., Pannella, M., Elbaz, D., et al. 2015, A&A, 575, A74
Scoville, N., Aussel, H., Brusa, M., et al. 2007, ApJS, 172, 1
Simpson, J. M., Smail, I., Swinbank, A. M., et al. 2015, ApJ, 807, 128
Simpson, J. M., Smail, I., Wang, W.-H., et al. 2017, ApJL, 844, L10
Simpson, J. M., Swinbank, A. M., Smail, I., et al. 2014, ApJ, 788, 125
Smail, I., Ivison, R. J., & Blain, A. W. 1997, ApJL, 490, L5
Smail, I., Ivison, R. J., Owen, F. N., Blain, A. W., & Kneib, J.-P. 2000, ApJ, 528, 612
Smolčić, V., Novak, M., Delvecchio, I., et al. 2017, A&A, 602, A6
Speagle, J. S., Steinhardt, C. L., Capak, P. L., & Silverman, J. D. 2014, ApJS, 214, 15
Surace, J. A., Sanders, D. B., & Evans, A. S. 2000, ApJ, 529, 170
Swinbank, A. M., Simpson, J. M., Smail, I., et al. 2014, MNRAS, 438, 1267

Swinbank, A. M., Smail, I., Chapman, S. C., et al. 2010, MNRAS, 405, 234
Tadaki, K.-i., Kodama, T., Nelson, E. J., et al. 2017, ApJL, 841, L25
Targett, T. A., Dunlop, J. S., Cirasuolo, M., et al. 2013, MNRAS, 432, 2012
Toft, S., Smolčić, V., Magnelli, B., et al. 2014, ApJ, 782, 68
Toft, S., van Dokkum, P., Franx, M., et al. 2007, ApJ, 671, 285
van der Wel, A., Bell, E. F., Häussler, B., et al. 2012, ApJS, 203, 24
van der Wel, A., Franx, M., van Dokkum, P. G., et al. 2014, ApJ, 788, 28
van Dokkum, P. G., Franx, M., Kriek, M., et al. 2008, ApJL, 677, L5

Veilleux, S., Kim, D.-C., & Sanders, D. B. 2002, ApJS, 143, 315
Wang, W.-H., Lin, W.-C., Lim, C.-F., et al. 2017, ApJ, 850, 37
Whitaker, K. E., Franx, M., Leja, J., et al. 2014, ApJ, 795, 104
Wiklind, T., Conselice, C. J., Dahlen, T., et al. 2014, ApJ, 785, 111
Zamojski, M., Yan, L., Dasyra, K., et al. 2011, ApJ, 730, 125
Zavala, J. A., Aretxaga, I., Dunlop, J. S., et al. 2018, MNRAS, 475, 5585
Zirm, A. W., van der Wel, A., Franx, M., et al. 2007, ApJ, 656, 66